Experimental and Numerical Studies of Laser-welded Stainless Steel I-section Beam-columns

Yidu Bu and Leroy Gardner

Imperial College London

Abstract

The stability and design of laser-welded stainless steel I-section beam-columns are explored in this study. Owing to the high precision and low heat input of laser-welding, structural cross-sections produced using this fabrication method have smaller heat affected zones, lower thermal distortions and lower residual stresses than would typically arise from traditional welding processes. Eighteen laser-welded stainless steel beam-columns were tested to investigate the member buckling behaviour under combined compression and bending. Two I-section sizes were considered in the tests: I-50×50×4×4 in grade EN 1.4301 and I-102×68×5×5 in grade EN 1.4571 stainless steel. The two cases of minor axis bending plus compression and major axis bending plus compression with lateral restraints were investigated. The initial loading eccentricities in the beam-column tests were varied to provide a wide range of bending moment-to-axial load ratios. The test results obtained herein and from a previous experimental study were used to validate finite element (FE) models, which were subsequently employed for parametric investigations to generate further structural performance data over a wider range of cross-section sizes, member lengths and loading combinations. The obtained test and FE results were utilized to evaluate the accuracy of the beam-column capacity predictions according to the current European code, American design guide and a recent proposal by Greiner and Kettler. Finally, an improved approach for the design of stainless steel I-section beam-columns is proposed.

Keywords

Beam-columns, Eurocode 3, Experiments, Laser-welding, Numerical modelling, Stainless steel, Testing

1 Introduction

Stainless steel is becoming increasingly used in the construction industry owing to its corrosion resistance, aesthetic appeal, favourable structural properties and a range of other beneficial characteristics. A recent addition to the stainless steel product range is that of laser-welded sections. Laser-welding is a fabrication method which uses lasers to locally melt and fuse together individual metallic elements into a range of complete structural sections without the use of filler material. Compared to conventional arc welding, laser-welding enables the heat input to be kept to a minimum, and thus leads to lower thermal distortions and residual stresses. Since their recent introduction to the construction industry, there has only been some initial research[1-4] into the structural behaviour of laser-welded stainless steel sections, and their design is not explicitly covered in current structural design provisions.

The design of beam-column members generally features interaction formulae, with the bending moment resistance and compressive member resistance as end points. Previous research has been carried out into the behaviour and cross-section resistance of stainless steel I-sections in bending[5-11] and the member buckling behaviour of stainless steel I-section members in compression[7, 12-15]. Research has been performed on stainless steel beam-columns, but focussing on hollow sections[16-19], while studies and data on I-section beam-column are scarce. In 2000, Burgan et al.[7] conducted eight stainless steel welded I-section beam-column tests under compression and major axis bending. More recently Zheng et al.[16] carried out five stainless steel welded I-section beam-column tests with different buckling lengths to investigate their global stability.

In this paper, experimental and numerical studies of the member buckling behaviour of laser-welded stainless steel I-section beam-columns are presented. A total of 18 tests, with a number of combinations of compression and bending about both the major and minor axes were carried out. Numerical models were developed to replicate the experimental responses, obtained from the tests performed herein and in a previous study[7], and subsequently employed in a comprehensive parametric study to generate further data over a broader range of cross-section slenderness, member slenderness and loading combinations. The test and numerical data were used to evaluate the accuracy of the codified design provisions for stainless steel I-section beam-columns, including those given in the European code EN 1993-1-4[20], AISC Design Guide 27[21], and the proposals by Greiner and Kettler[22]. An improved approach for the design of stainless steel I-section beam-columns is then proposed.

2 Experimental Investigation

An experimental programme was carried out in order to study the behaviour of stainless steel I-section beam-columns. Two cross-section sizes were considered: I-50×50×4×4 in grade 1.4301 stainless steel and I-102×68×5×5 in grade 1.4571 stainless steel. The cross-sections were laser-welded from hot-rolled stainless steel plates. The cross-sections (e.g. I-50×50×4×4) are designated as follows: I-section height (h) × section width (b_f) × web thickness (t_w) × flange thickness (t_f). Both of the cross-sections are Class 1, according to the slenderness limits set out in EN 1993-1-4[20]. Measurements of material properties, initial geometric imperfections and residual stresses were also made. The experimental procedures and key results obtained are reported in this section.

2.1 Material properties and residual stresses

Measurements were taken of both the tensile and compressive material stress-strain properties of the test specimens. Tensile properties were determined from coupon tests conducted in accordance with EN ISO 6892-1[23], while compressive properties were derived from stub column tests, as described in [1], where the compound Ramberg-Osgood model that utilises the 0.2% proof stress f_y and 1.0% proof stress $f_{1.0}$[24] was fitted to the available stress-strain data prior to the onset of local buckling, and extrapolated up to the ultimate tensile stress beyond this point.

A summary of the key measured properties is given in Table 1, where E is the Young's modulus, f_y is the 0.2% proof stress, $f_{1.0}$ is the 1.0% proof stress, f_u is the ultimate stress, ε_u is the strain at the ultimate stress, ε_f is the strain at fracture, measured over the standard gauge length, and n, $n_{0.2,1.0}$ and $n_{0.2,u}$ are the strain hardening exponents for the compound Ramberg-Osgood model[24]. The subscript ‘c’ denotes compressive properties.

Table 1 Summary of tensile and compressive material properties

Cross-section	***E* (N/mm^2)**	**f_y (N/mm^2)**	**$f_{1.0}$ (N/mm^2)**	**f_u (N/mm^2)**	**ε_u (%)**	**ε_f (%)**	**Compound R-O coefficients**		
							n	**$n_{0.2,1.0}$**	**$n_{0.2,u}$**
I-50×50×4×4	190700	270	361	694	61	73	4.0	3.2	3.0
I-102×68×5×5	186800	222	331	580	50	64	3.2	3.9	3.8
Cross-section	E_c (N/mm^2)	$f_{y,c}$ (N/mm^2)	$f_{1.0,c}$ (N/mm^2)	$f_{u,c}$ (N/mm^2)	$\varepsilon_{u,c}$ (%)	$\varepsilon_{f,c}$ (%)	Compound R-O coefficients		
							n_c	$n_{0.2,1.0,c}$	$n_{0.2,u,c}$
I-50×50×4×4	206900	332	402	694	61	-	7.4	3.2	3.0
I-102×68×5×5	190800	291	354	580	50	-	6.4	3.9	3.8

2.2 Residual stresses

The residual stress patterns in the tested laser-welded cross-sections were measured using the sectioning method following the procedures recommended by the Structural Stability Research Council[25]. The test specimens were divided into strips and by measuring the change in the length of the strips, the strain relieved during sectioning was obtained. The residual stresses were then determined by multiplying the released strains by the Young's modulus. Based on the measured residual stresses distributions in laser-welded stainless steel I-sections obtained in [1] and T-sections obtained in [26], a predictive pattern of residual stresses was proposed for laser-welded austenitic stainless steel cross-sections in [1]. The proposed generic distribution, together with the definition of the symbols, is illustrated in Fig. 1, while the key parameters are shown in Table 2. Equivalent parameters for conventionally welded austenitic stainless steel[27] and carbon steel[28, 29] I-sections are also listed for comparison. As expected, lower levels of residual stress were found in the laser-welded sections than typically arise in conventionally welded sections due to the lower thermal input associated with laser-welding. The residual stress pattern set out in Fig. 1 and Table 2 is adopted in the numerical study presented in Section 3 of this paper.

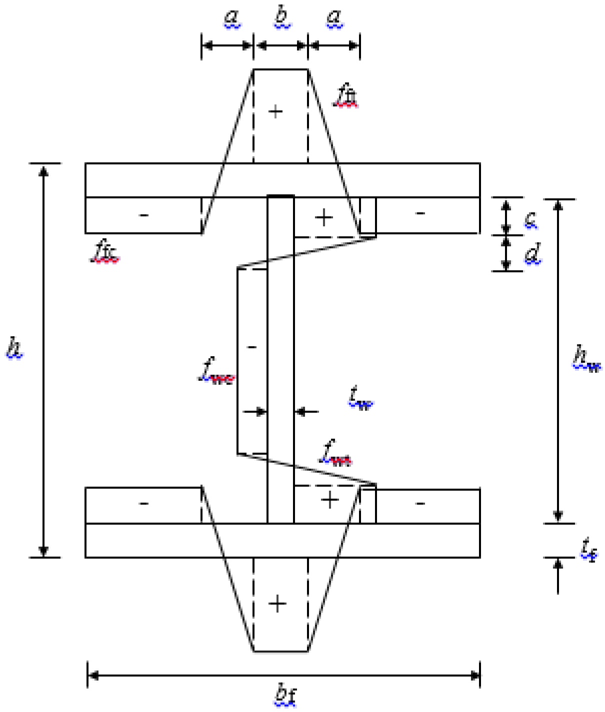

Fig. 1 General residual stress distribution for welded I-sections (+ve=tension;-ve=compression)

Table 2 Parameters in predictive models for welded I-sections

Predictive model	$f_{ft} = f_{wt}$	$f_{fc} = f_{wc}$	*a*	*b*	*c*	*d*
Gardner et al.[1]	$0.5f_y$	From equilibrium	$0.1b_f$	$0.075b_f$	$0.025h_w$	$0.05h_w$
Yuan et al.[27]	$0.8f_y$	From equilibrium	$0.225b_f$	$0.05b_f$	$0.025h_w$	$0.225h_w$
ECCS[28]	f_y	$0.25f_y$	$0.05b_f$	$0.15b_f$	$0.075h_w$	$0.05h_w$
BSK 99[29]	$0.5f_y$	From equilibrium	$0.75t_f$	$1.5t_f$	$1.5t_w$	$1.5t_w$

2.3 Minor axis bending plus compression tests

In total, twelve beam-columns under combined axial compression and bending about the minor axis were tested to study their structural behaviour and load-carrying capacity. Two cross-sections were investigated (I-102×68×5×5 and I-50×50×4×4). For each cross-section size, all the specimens had a fixed nominal length, with a range of six initial loading eccentricities to give a spectrum of bending moment-to-axial load ratios. Prior to the welding of the 12 mm thick end plates, the geometric dimensions of the beam-column specimens were measured. The initial global geometric imperfection amplitudes w_g in the direction of buckling were also measured using a self-levelling laser. Initial local geometric imperfections were not measured for each test specimen, but representative magnitudes (w_l=0.23 mm for I-50×50×4×4 and w_l=0.22 mm for I-102×68×5×5) for the two tested cross-section sizes were obtained previously [1]. The geometric dimensions and maximum global geometric imperfections are reported in Table 3.

The tests were performed using a 2000 kN Instron servo-hydraulic testing machine under displacement control at a constant rate of approximately 0.4 mm/min. Pin-ended conditions at the top and bottom of the members were achieved through a pair of knife edges and wedge plates, as shown in

Fig. 2. This resulted in the members being pinned about the minor axis and fixed about the major axis. In the experimental procedure, each specimen was first put into position with the desired initial loading eccentricity (i.e. the relative distance between the centreline of the specimen and the knife-edges). The specimens were then secured in position by clamps.

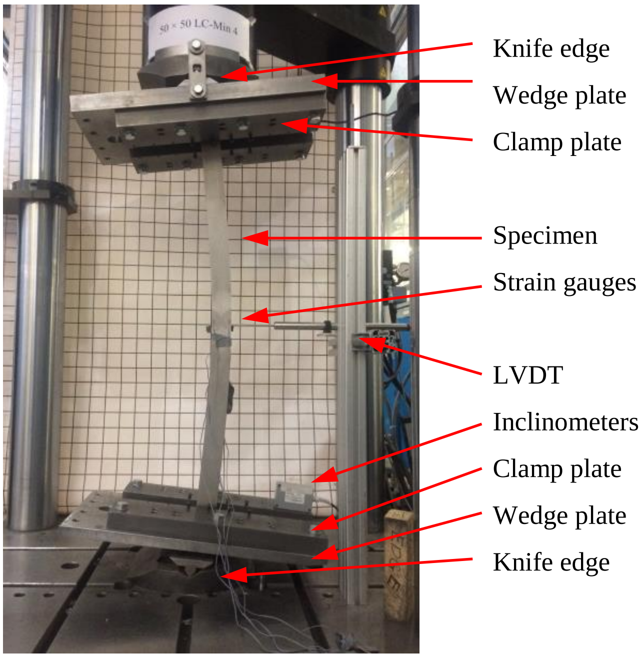

Fig. 2 Test configuration for specimens under combined axial compression and minor axis bending

A linear variable differential transformer (LVDT) was placed at the mid-height of the specimens to measure the lateral deflection. Two inclinometers were positioned at the top and bottom wedge plates to measure the end rotations, while the end shortening of the specimens was measured by means of an LVDT within the testing machine. Four strain gauges were affixed at a distance of d_s (10 mm for cross-section I-102×68×5×5 and 5 mm for cross-section I-50×50×4×4) from the outer edge of each flange (as shown in Fig. 3) at the mid-height of each specimen so that the longitudinal strains at the maximum compressive fibre ε_{max} and the maximum tensile (or the minimum compressive, in some cases) fibre ε_{min} could be calculated. The strain gauge values were used to determine the initial loading eccentricities using the method described by Zhao et al. [30]. The calculation was carried out according to Equations (1) to (3), in which I is the second moment of area about the buckling axis, ε_1, ε_2, ε_3 and ε_4 are the strain gauge values, δ is the lateral deflection at mid-height, w_g is the

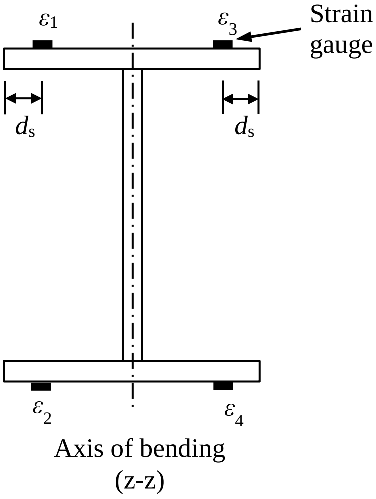

initial global imperfection at mid-height and N is the applied load. The determined eccentricities are later employed in the numerical modelling in Section 3 and the design calculations in Section 4. All data were recorded using the DATASCAN data acquisition system at 1 second intervals.

$$\varepsilon_{max} = (\varepsilon_1+\varepsilon_2)/2, \tag{1}$$

$$\varepsilon_{min} = (\varepsilon_3+\varepsilon_4)/2, \tag{2}$$

$$e_0 = \frac{EI(\varepsilon_{max}-\varepsilon_{min})}{N(b_f-2d_s)}-\delta-\omega_g. \tag{3}$$

Fig. 3 Strain gauge arrangement for specimens under combined axial compression and minor axis bending

The measured geometric properties and initial global imperfection amplitudes for each specimen are reported in Table 3, where L_{cr} is the effective member length (measured between the knife-edges), h is the section height, b_f is the section width, t_w is the web thickness, t_f is the flange thickness and $\bar{\lambda} = \sqrt{Af_y/N_{cr}}$ is the member non-dimensional slenderness, where A is the cross-section area and $N_{cr} = \pi^2 EI/L_{cr}^2$ is the Euler buckling load about the buckling axis. The key results obtained from the minor axis beam-column tests are summarised in Table 4. The initial calculated (actual) loading eccentricity from the strain gauges e_0, the total actual initial load eccentricity (e_0+w_g), the ultimate vertical load $N_{u,test}$, the ultimate first order bending moment $M_{u,test} = N_{u,test}(e_0+w_g)$ and the mid-height lateral deflection at the peak load $\delta_{u,test}$ are presented.

Table 3 Measured geometric properties of beam-column specimens under compression and minor axis bending

Cross-section	Specimen ID	h (mm)	b_f (mm)	t_w (mm)	t_f (mm)	L_{cr} (mm)	$\bar{\lambda}_z$	ω_g (mm)
I-102×68×5×5	102Min1	101.90	68.01	5.05	5.07	1272.9	1.04	0.33
I-102×68×5×5	102Min2	102.14	67.97	4.99	5.09	1272.2	1.04	0.58
I-102×68×5×5	102Min3	102.16	68.00	4.95	5.07	1272.2	1.04	0.17
I-102×68×5×5	102Min4	101.91	67.99	5.00	5.07	1274.2	1.04	0.63
I-102×68×5×5	102Min5	101.97	67.99	5.02	5.05	1271.8	1.04	0.02
I-102×68×5×5	102Min6	101.99	67.97	4.98	5.06	1273.9	1.04	0.22
I-50×50×4×4	50Min1	50.40	50.53	4.01	4.00	1163.0	1.21	0.33
I-50×50×4×4	50Min2	50.55	50.56	4.03	4.02	1163.4	1.21	0.18
I-50×50×4×4	50Min3	50.31	50.56	3.92	3.97	1162.9	1.21	0.17
I-50×50×4×4	50Min4	50.46	50.55	3.97	3.98	1163.3	1.21	0.23
I-50×50×4×4	50Min5	50.44	50.53	4.01	4.00	1163.1	1.21	0.31
I-50×50×4×4	50Min6	50.32	50.59	4.04	3.94	1162.8	1.21	0.41

Table 4 Summary of minor axis beam-column test results

Cross-section	Specimen ID	e_0 (mm)	(e_0+w_g) (mm)	$N_{u,test}$ (kN)	$M_{u,test}$ (kNm)	$\delta_{u,test}$ (mm)
I-102×68×5×5	102Min1	0.17	0.50	185.26	0.09	5.97
	102Min2	3.85	4.43	138.96	0.62	11.33
	102Min3	10.15	10.32	109.54	1.13	14.01
	102Min4	19.67	20.30	77.47	1.57	17.79
	102Min5	43.56	43.58	49.54	2.16	24.88
	102Min6	80.90	81.12	30.22	2.45	27.38
I-50×50×4×4	50Min1	0.72	1.05	82.09	0.09	6.93
	50Min2	5.36	5.54	61.54	0.34	10.82
	50Min3	11.04	11.21	48.32	0.54	13.11
	50Min4	21.69	21.92	34.24	0.75	18.32
	50Min5	42.41	42.72	22.30	0.95	24.58
	50Min6	80.32	80.73	13.59	1.10	32.22

The load–mid-height lateral deflection curves are shown in Figs. 4 and 5 for the I-102×68×5×5 and I-50×50×4×4 specimens, respectively. All the specimens failed by a combination of bending and flexural buckling about the minor axis, with no evidence of local buckling or out-of-plane deformations, as shown in Fig. 6.

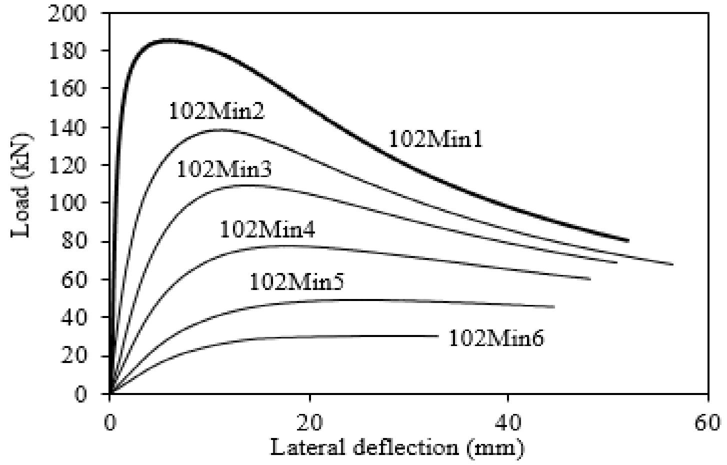

Fig. 4 Load–mid-height lateral deflection curves for beam-column tests under combined axial compression and bending about the minor axis (I-102×68×5×5)

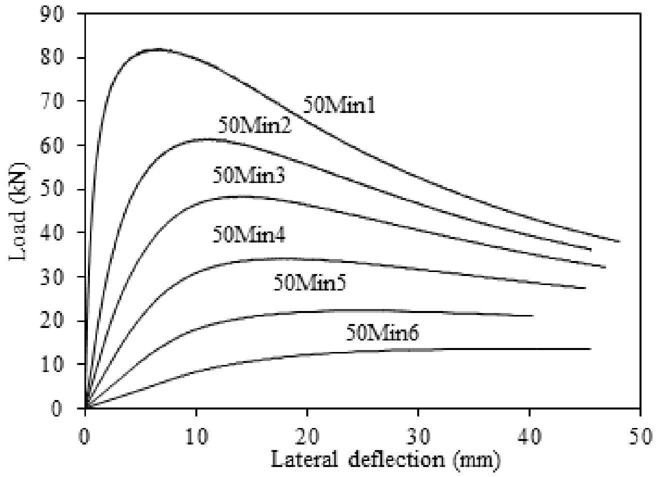

Fig. 5 Load–mid-height lateral deflection curves for beam-column tests under combined axial compression and bending about the minor axis (I-50×50×4×4)

Fig. 6 Typical failure mode for beam-column under combined axial compression and bending about the minor axis (50Min4)

2.4 Major axis bending plus compression tests (with lateral restraints)

Beam-columns under combined axial compression and bending about major axis were tested following the same procedure as described in Section 2.3. Six tests were carried out on cross-section I-50×50×4×4, with a range of initial loading eccentricities. Similar to the tests in bending about the minor axis, the geometric dimensions and maximum global geometric imperfections were measured and are reported in Table 5. Knife edges were employed to achieve pinned end conditions about the major axis and fixed end conditions about the minor axis. Lateral restraints were provided to all specimens to prevent minor axis deflections. The lateral restraint system comprised three sets of horizontal tubes at the quarter points of the specimen and diagonal bracing to enhance the out-of-plane stiffness of the system, as shown, along with the general test setup, in Fig. 7. One extra LVDT was used to measure the out-of-plane displacement, but the recording was found to be negligible, showing that the lateral restraint system was effective. For the beam-columns under compression and major axis bending, strain gauges were attached to the centre of each flange at the mid-height of the specimens, recording the longitudinal strains at the maximum compressive fibre ε_{max} and the maximum tensile (or the minimum compressive, in some cases) fibre ε_{min}, as shown in Fig. 8. The actual initial loading eccentricities e_0 were calculated according to Equation (4),

$$e_0 = \frac{EI(\varepsilon_{max} - \varepsilon_{min})}{Nh} - \delta - \omega_g. \tag{4}$$

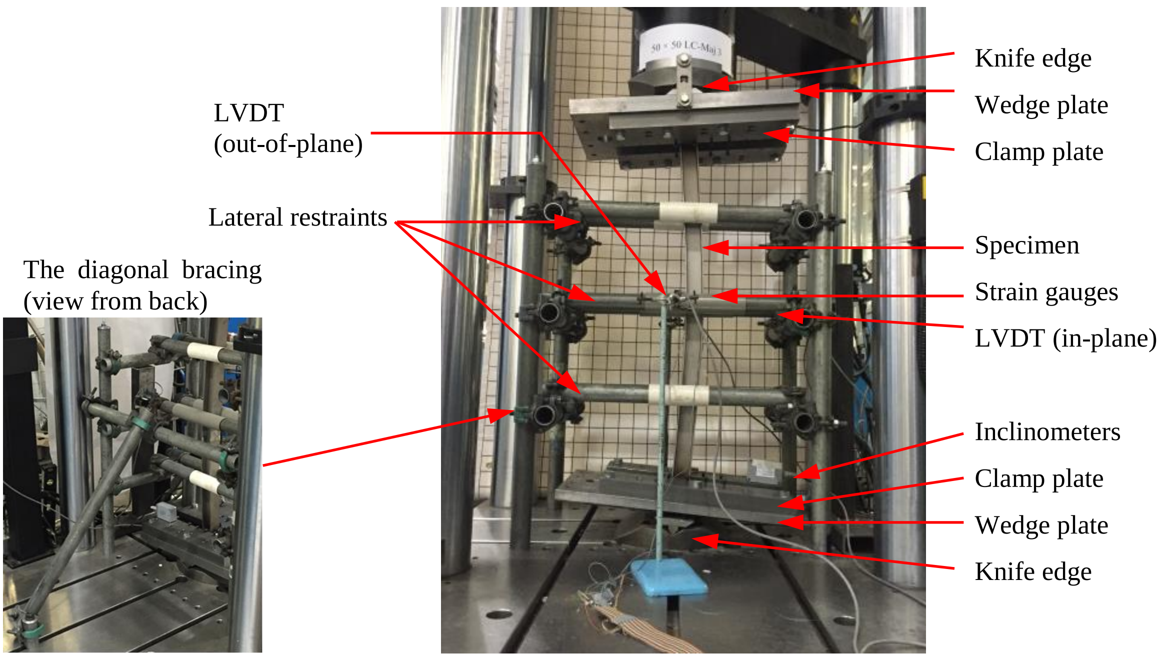

Fig. 7 Test configurations for specimen under combined axial compression and major axis bending

Table 5 Measured geometric properties of beam-column specimens under compression and major axis bending

Cross-section	Specimen ID	h (mm)	b_f (mm)	t_w (mm)	t_f (mm)	L_{cr} (mm)	$\bar{\lambda}_y$	ω_g (mm)
I-50×50×4×4	50Maj1	50.35	50.52	3.99	3.98	1162.8	0.72	0.18

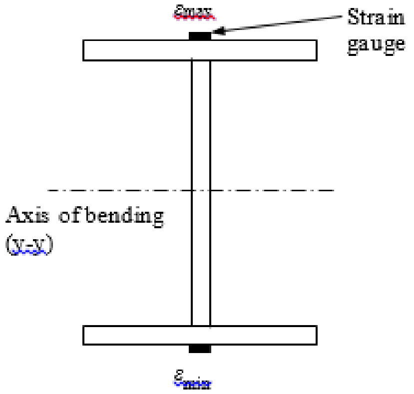

I-50×50×4×4	50Maj2	50.39	50.58	3.98	3.99	1163.1	0.72	0.19
I-50×50×4×4	50Maj3	50.36	50.57	3.99	4.00	1162.7	0.72	0.10
I-50×50×4×4	50Maj4	50.34	50.54	3.99	3.97	1162.9	0.72	0.19
I-50×50×4×4	50Maj5	50.30	50.59	3.99	3.99	1163.1	0.72	0.12
I-50×50×4×4	50Maj6	50.36	50.61	4.01	4.04	1162.9	0.72	0.10

Fig. 8 Strain gauge arrangement for specimens under combined axial compression and major axis bending

The key results obtained from the major axis beam-column tests are summarised in Table 6, while the load–mid-height lateral deflection responses are shown in Fig. 9. All the specimens failed by a combination of bending and flexural buckling about the major axis, as depicted in Fig. 10 for a typical specimen.

Table 6 Summary of major axis bending beam-column test results

Cross-section	Specimen ID	e_0 (mm)	(e_0+w_g) (mm)	$N_{u,test}$ (kN)	$M_{u,test}$ (kNm)	$\delta_{u,test}$ (mm)
I-50×50×4×4	50Maj1	0.09	0.27	147.53	0.01	3.89
	50Maj2	4.77	4.96	114.28	0.55	8.41
	50Maj3	9.78	9.88	93.18	0.91	11.48
	50Maj4	20.08	20.27	72.80	1.46	15.34
	50Maj5	40.06	40.18	48.52	1.94	21.56
	50Maj6	80.10	80.20	33.01	2.64	33.08

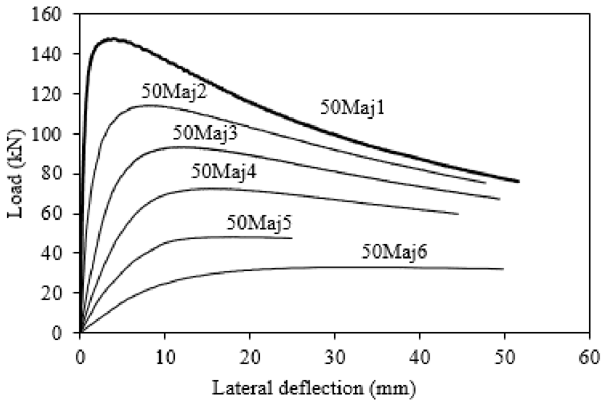

Fig. 9 Load–mid-height lateral deflection curves for beam-column tests under combined axial compression and bending about the major axis

Fig. 10 Typical failure mode for beam-column under combined axial compression and bending about the major axis (50Maj5)

3 Numerical Modelling

3.1 Introduction

A numerical modelling study of the laser-welded stainless steel beam-columns was conducted, using the general-purpose finite element analysis package ABAQUS[31], to supplement the experimental data. The experimental results were used to validate the FE models. Upon validation, the models were employed in parametric studies which expanded the current data pool over a wider range of cross-section sizes, cross-section slenderness, member slenderness, and loading combinations.

3.2 Modelling assumptions

The shell element S4R[31], which is a four-noded doubly curved general-purpose shell element, was adopted to discretise the beam-columns. This element type has been successfully employed in previous numerical studies of thin-walled structures[9, 17, 32, 33]. The mesh size of the cross-sections was set equal to the wall thickness, providing accurate results in practical computational times. The measured geometric dimensions and obtained compressive material properties were employed in the finite element models to replicate the corresponding test behaviour.

The measured engineering stress-strain response (σ_{nom}-ε_{nom}) was represented by the two stage Ramberg-Osgood model[24] and converted into true stress-log plastic strain (σ_{true}-ε_{ln}^{pl}) using Equations (5) and (6) before input into ABAQUS in multi-linear form with 50 intervals. Note that Equations (5) and (6) are correct for the conversion of tensile material properties, while for compression, either the engineering strain values ε_{nom} should be taken as negative or, if using absolute values, the (1+ε_{nom}) term should be changed to (1-ε_{nom}).

$$\sigma_{true} = \sigma_{nom}(1+\varepsilon_{nom}) \,, \tag{5}$$

$$\varepsilon_{ln}^{pl} = \ln(1+\varepsilon_{nom}) - \frac{\sigma_{true}}{E} \,. \tag{6}$$

The boundary conditions were carefully selected to simulate the experimental set-up. All nodes at each end section were coupled to an eccentric reference point. The rotation about the axis of bending at both ends and the longitudinal translation at the loaded end were released to simulate the pin-ended boundary conditions. Moreover, the eccentric reference points were offset longitudinally from each end by 75 mm, simulating the distance from the specimen end to the knife-edge tip in the tests.

3.3 Initial geometric imperfections and residual stresses

Initial geometric imperfections were incorporated in the models in the form of the lowest local and global eigenmodes, with different amplitudes. The elastic buckling mode shapes were determined by a prior eigenvalue buckling analysis and were scaled with three imperfection amplitude combinations: (a) the measured global and local imperfection amplitudes w_g+w_l, where the values of w_g are reported in Tables 3 and 5 and the values of w_l were described in Section 2.3, (b) L_{cr}/1000+t_f/100, and (c) L_{cr}/1000+$w_{D\&W}$, where $w_{D\&W}$ is the modified Dawson and Walker imperfection amplitude[34] as given by Equation (7):

$$w_{\mathrm{D\&W}} = 0.023\left(\frac{f_{\mathrm{y,c}}}{f_{\mathrm{cr}}}\right)t, \tag{7}$$

where f_{cr} is the elastic critical buckling stress of the most slender constituent element in the cross-section and t is the thickness of the element. The measured initial load eccentricities e_0 from Tables 4 and 6 were used in all cases. The residual stress pattern presented in Table 2 was also applied to the models using the *INITIAL CONDITIONS feature. Considering both geometrical and material nonlinearities, the FE models were solved by means of the modified Riks method[31] to trace the full load-deformation histories of the models.

3.4 Validation of the numerical models

The accuracy of the developed beam-column FE models was assessed through a series of comparisons between the test and FE results. The experimental results obtained in Section 2 of this paper and from a previous experimental study [7] on welded stainless steel I-section beam-columns were employed for the validation. The ultimate loads obtained from the FE models $N_{u,FE}$ were compared to those from the corresponding experiments $N_{u,test}$, for beam-columns bending about the minor and major axis, in Tables 7 and 8, respectively. The ratios of experimental to numerical failure loads ($N_{u,test}/N_{u,FE}$) for the three imperfection combinations described in Section 3.3 are presented. Note that for the experimental results reported in [7], imperfection measurement were not reported so combination (a) was not assessed, and the residual stress distribution from Table 2 for conventional welding was adopted.

It can be seen that the test failure loads are well predicted by the developed numerical models for all three considered combinations of global and local imperfection amplitudes. Typical failure modes obtained from the FE models and those observed in the tests for beam-columns bending about the minor and major axes are presented in Figs. 11 and 12, respectively. The corresponding load–mid-height lateral deflection curves derived from the FE models are plotted with their experimental counterparts in Figs. 13 and 14, respectively. Overall, the developed numerical models may be seen to capture the behaviour and results obtained in the tests accurately.

Table 7 Comparison of test and FE results with different imperfection combinations for beam-columns under compression and bending about the minor axis

Cross-section	References	Specimen ID	$N_{u,test}/N_{u,FE}$		
			w_g+w_l	$L_{cr}/1000+t_f/100$	$L_{cr}/1000+w_{D\&W}$
I-102×68×5×5	Section 2 of this paper	102Min1	1.03	1.04	1.04
		102Min2	1.05	1.05	1.05
		102Min3	1.09	1.09	1.09
		102Min4	1.04	1.04	1.04
		102Min5	1.04	1.05	1.05
		102Min6	0.97	0.98	0.98
I-50×50×4×4	Section 2 of this paper	50Min1	1.02	1.02	1.02
		50Min2	1.03	1.05	1.05
		50Min3	1.05	1.05	1.05
		50Min4	1.02	1.03	1.03
		50Min5	0.98	0.98	0.98
		50Min6	0.93	0.93	0.93
Mean			1.02	1.03	1.02
COV			0.04	0.04	0.04

Table 8 Comparison of test and FE results with different imperfection combinations for beam-columns under compression and bending about the major axis

Cross-section	References	Specimen ID	$N_{u,test}/N_{u,FE}$		
			w_g+w_l	$L_{cr}/1000+t_f/100$	$L_{cr}/1000+w_{D\&W}$
I-50×50×4×4	Section 2 of this paper	50Maj1	1.07	1.09	1.09
		50Maj2	1.06	1.09	1.09
		50Maj3	1.01	1.05	1.05
		50Maj4	1.01	1.03	1.03
		50Maj5	0.93	0.97	0.97
		50Maj6	1.01	1.03	1.03
I-160×80×6×10	Burgan et al.[7]	I-160×80-EC0	-	1.05	1.05
		I-160×80-EC1	-	0.98	0.98
		I-160×80-EC2	-	0.96	0.96
		I-160×80-EC3	-	1.05	1.05
I-160×160×6×10		I-160×160-EC0	-	0.95	0.95
		I-160×160-EC1	-	0.99	0.98
		I-160×160-EC2	-	0.95	0.94
		I-160×160-EC3	-	0.98	0.98
Mean			1.02	1.01	1.01
COV			0.05	0.05	0.05

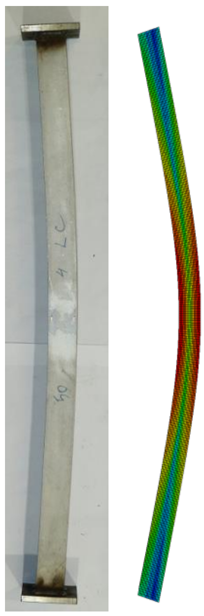

Fig. 11 Experimental and numerical failure modes for beam-column specimen 50Min4 under compression and bending about the minor axis

Fig. 12 Experimental and numerical failure modes for beam-column specimen 50Maj5 under compression and bending about the major axis

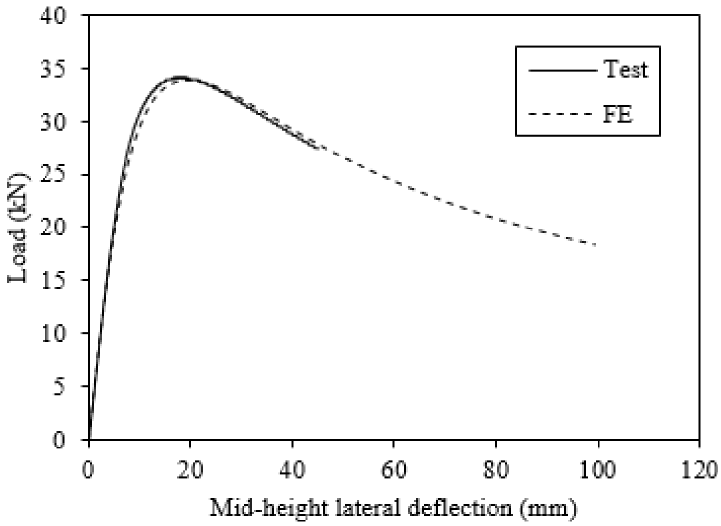

Fig. 13 Experimental and numerical load–mid-height lateral deflection curves for specimen 50Min4 under compression and bending about the minor axis

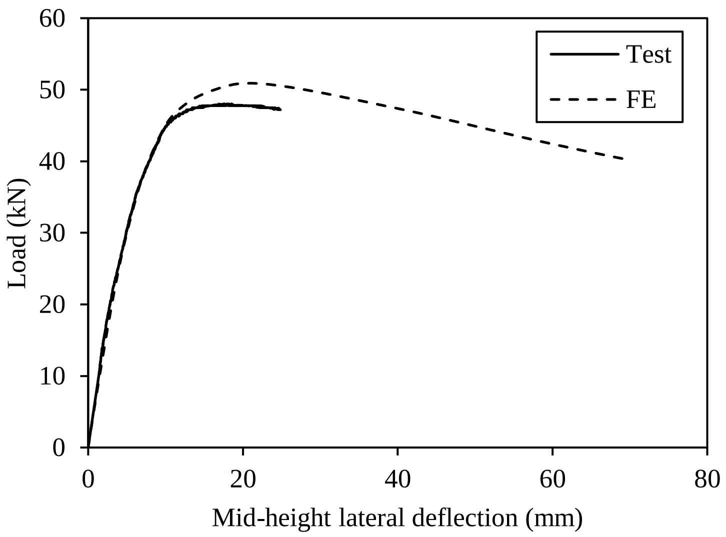

Fig. 14 Experimental and numerical load–mid-height lateral deflection curves for specimen 50Maj5 under compression and bending about the major axis

3.5 Parametric study

Upon validation of the FE models, a series of parametric studies was carried out to generate beam-column data over a wider range of cross-section sizes, cross-section slenderness, member slenderness, and loading combinations. The compressive material properties of specimen I-102×68×5×5 were adopted throughout the parametric studies.

In total, 960 parametric results were generated covering beam-columns in compression and bending about both the major and minor axes. The cross-section height (100 mm) was kept constant, while the flange width was varied to generate four aspect ratios h/b (1.0, 1.5, 2.0 and 3.0). The thicknesses of the flanges and web were varied to cover a range of plate slendernesses while, at the same time, retaining similar values for the flange slenderness $\bar{\lambda}_{p,f}$ and the web slenderness $\bar{\lambda}_{p,w}$ which are defined, in accordance with [20], by Equations (8) and (9):

$$\bar{\lambda}_{p,f} = \sqrt{f_y / f_{cr,f}}, \tag{8}$$

$$\bar{\lambda}_{p,w} = \sqrt{f_y / f_{cr,w}}, \tag{9}$$

where $f_{cr,f}$ and $f_{cr,w}$ are the elastic buckling stresses of the flange and web, considered in isolation.

For each cross-section, beam-column models with six different lengths were generated to give a spread of non-dimensional member slenderness values $\bar{\lambda}$ from 0.4 to 2.0. For each case, a range of initial loading eccentricities (0 mm to 80 mm) was employed to provide a range of axial load-to-bending moment ratios. Initial global and local geometric imperfections based on the lowest respective eigenmodes, with the amplitudes of $L_{cr}/1000$ and $t_f/100$ were included in the models. The laser-welded residual stress pattern from Section 2.1 was used in all simulations. The results are summarised in Section 4 and employed to assess the existing design approaches for stainless steel I-section beam-columns.

4 Discussion and Assessment of Current Design Methods

4.1 Introduction

The accuracy of three existing design approaches for stainless steel I-section beam-columns, as set out in the European code EN 1993-1-4[20], AISC Design Guide 27[21] and a recent proposal by Greiner and Kettler[22], are examined. The ratios of the experimental (or numerical) failure loads to the predicted failure loads from each design method $N_u/N_{u,pred}$ are reported in Tables 9 and 10, for Class 1 and 2 and Class 3 cross-sections, respectively. The predicted failure loads were obtained assuming proportional loading, following a similar procedure to that reported in [35], where N_u is the ultimate axial load obtained from the test (or FE model) corresponding to the distance on the N-M interaction curve from the origin to the test (or FE) data point and $N_{u,pred}$ is the predicted axial load corresponding to the distance from the origin to the intersection with the design interaction curve. An angle parameter θ is introduced to describe the loading combination of axial load and bending moment within one variable, as illustrated in Fig. 15; as the applied loading changes from pure bending to pure compression θ changes from 0° to 90°. The angle θ can be calculated from Equation (10),

$$\theta = \tan^{-1}\left(\frac{N/N_R}{M/M_R}\right), \tag{10}$$

where N_R and M_R are the codified column buckling strength and bending moment capacity, respectively and represent the end points of the N-M interaction curve. A value of $N_u/N_{u,pred}$ greater than unity indicates that the prediction is on the safe side. All the calculations are based on the measured (or modelled) geometric and material properties, and all partial factors are set to unity.

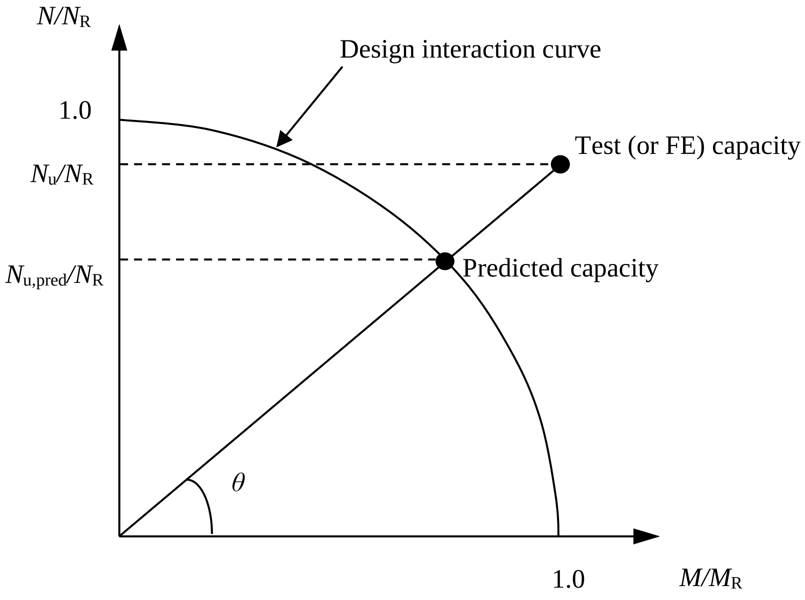

Fig. 15 Definition of θ on axial load–moment interaction curve

Table 9 Comparison of beam-column test and FE results with predicted strengths for Class 1 or 2 cross-sections

Loading combinations	No. of tests: 18 No. of simulations: 600	$N_u/N_{u,EC3}$	$N_u/N_{u,AISC}$	$N_u/N_{u,G\&K}$
Compression and bending about minor axis	Mean	1.21	1.06	1.18
	COV	0.13	0.18	0.12
Compression and bending about major axis	Mean	1.12	1.17	1.11
	COV	0.06	0.18	0.05

Table 10 Comparison of beam-column test and FE results with predicted strengths for Class 3 cross-sections

Loading combinations	No. of tests: 0 No. of simulations: 360	$N_u/N_{u,EC3}$	$N_u/N_{u,AISC}$	$N_u/N_{u,G\&K}$
Compression and bending about minor axis	Mean	1.28	1.29	-
	COV	0.09	0.14	-
Compression and bending about major axis	Mean	1.11	1.28	-
	COV	0.06	0.15	-

4.2 European code EN 1993-1-4 (EC3)

In the current European code EN 1993-1-4[20] for stainless steel, the format of the beam-column interaction formulae follows that used in EN 1993-1-1[36] for carbon steel, as given by Equations (11) and (12), with modified interaction buckling factors k_i to consider the effects of the material response of stainless steel on member instability, as given by Equations (13) and (14).

$$\frac{N_{Ed}}{(N_{b,Rd})_{min}}+k_z\left(\frac{M_{z,Ed}+N_{Ed}e_{Nz}}{\beta_{W,z}W_{pl.z}f_y/\gamma_{M1}}\right)\leq 1, \tag{11}$$

$$\frac{N_{Ed}}{(N_{b,Rd})_{min}}+k_y\left(\frac{M_{y,Ed}+N_{Ed}e_{Ny}}{\beta_{W,y}W_{pl,y}f_y/\gamma_{M1}}\right)\leq 1, \tag{12}$$

where N_{Ed} is the design axial load, $(N_{b,Rd})_{min}$ is the smallest design column buckling resistance for the four buckling modes: flexural buckling about the y axis, flexural buckling about the z axis, torsional buckling and torsional-flexural buckling, $M_{z,Ed}$ and $M_{y,Ed}$ are the design maximum first order bending moments about the minor and major axis respectively, e_{Nz} and e_{Ny} are the shifts in the neutral axes when the cross-section is subjected to uniform compression, and are equal to zero for I-sections, $W_{pl,z}$ and $W_{pl,y}$ are the plastic section moduli about the minor and major axes, respectively, $\beta_{W,z}$ and $\beta_{W,y}$ are parametrers which are equal to unity for Class 1 or 2 sections, the ratio of elastic to plastic moduli for Class 3 sections and the ratio of effective to plastic moduli for Class 4 cross-sections, and k_z and k_y are the interaction factors, as defined in Equations (13) and (14), respectively.

$$k_z = 1.0+2(\bar{\lambda}_z-0.5)\frac{N_{Ed}}{(N_{b,Rd})_{min1}}, \text{ but } 1.2 \le k_z \le 1.2+2\frac{N_{Ed}}{(N_{b,Rd})_{min1}}, \tag{13}$$

$$k_y = 1.0+2(\bar{\lambda}_y-0.5)\frac{N_{Ed}}{N_{b,y,Rd}}, \text{ but } 1.2 \le k_y \le 1.2+2\frac{N_{Ed}}{N_{b,y,Rd}}, \tag{14}$$

where $(N_{b,Rd})_{min1}$ is the smallest design column buckling resistance among flexural buckling about the z axis, torsional buckling and torsional-flexural buckling.

The obtained experimental and numerical results are compared with the Eurocode capacity predictions in

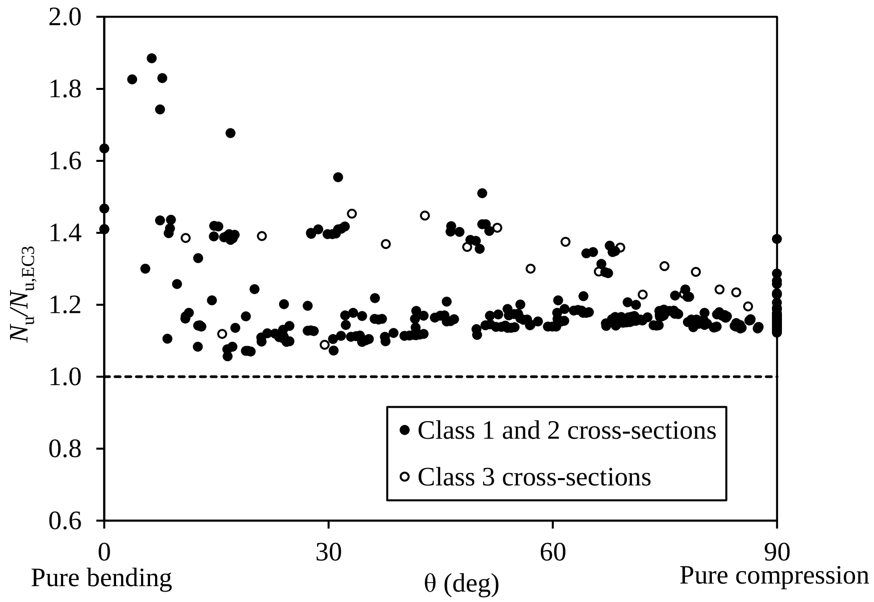

Fig. 16 for compression plus minor axis bending and Fig. 17 for compression plus major axis bending, where the test (or FE) to EC3 predicted failure load ratio $N_u/N_{u,EC3}$ is plotted against the angle parameter θ. Experimental results from previous studies[3,16] were also included, in all the comparisons in Sections 4 and 5. The comparison of test (or FE) results and EC3 predictions is reported in Table 9 and Table 10. The mean $N_u/N_{u,EC3}$ ratios are equal to 1.21 and 1.12, with coefficients of variations (COV) equal to 0.13 and 0.06, for Class 1 and 2 stainless steel I-section beam-columns under compression plus minor and major axis bending, respectively. For the beam-columns with Class 3 cross-sections, the mean $N_u/N_{u,EC3}$ ratios are equal to 1.28 and 1.11, with coefficients of variations (COV) equal to 0.09 and 0.06, under compression plus minor and major axis bending, respectively. Overall, the European code offers reasonable strength predictions, but there is clearly scope for improved accuracy and consistency, which is explored in Section 5 of this paper.

Fig. 16 Comparison of EC3 strength predictions with beam-column test and FE results under compression and minor axis bending

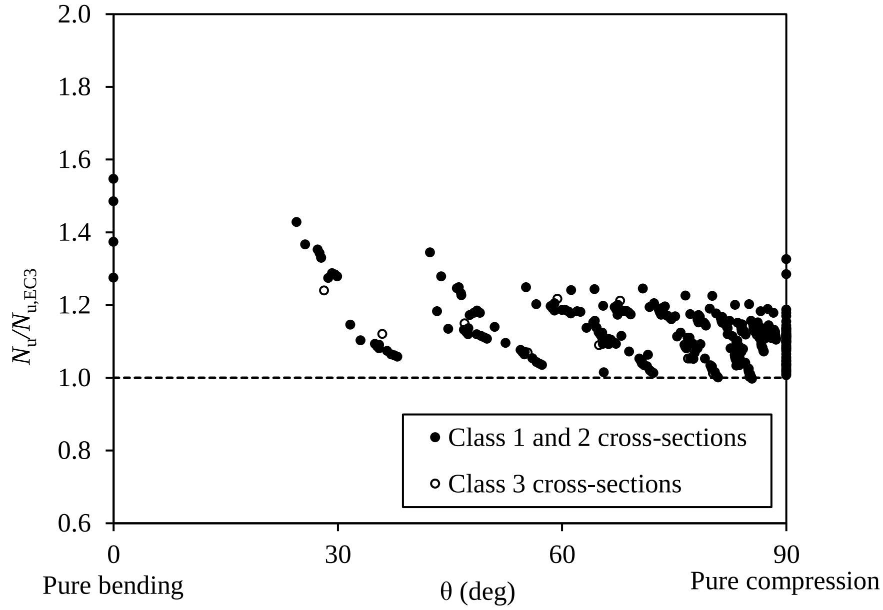

Fig. 17 Comparison of EC3 strength predictions with beam-column test and FE results under compression and major axis bending

4.3 AISC Design Guide 27

The AISC Design Guide 27[21] employs a pair of interaction formulae for doubly symmetric stainless steel members subjected to the combined actions of compression and bending moment, as given by Equations (15) and (16),

$$\frac{N_{\mathrm{Ed}}}{N_{\mathrm{c}}}+\frac{8}{9}\left(\frac{M_{\mathrm{z,Ed}}}{M_{\mathrm{z,c}}}+\frac{M_{\mathrm{y,Ed}}}{M_{\mathrm{y,c}}}\right)\leq 1,\ \text{for}\ \frac{N_{\mathrm{Ed}}}{N_{\mathrm{c}}}\geq 0.2, \tag{15}$$

$$\frac{N_{\mathrm{Ed}}}{2N_{\mathrm{c}}}+\left(\frac{M_{\mathrm{z,Ed}}}{M_{\mathrm{z,c}}}+\frac{M_{\mathrm{y,Ed}}}{M_{\mathrm{y,c}}}\right)\leq 1,\ \text{for}\ \frac{N_{\mathrm{Ed}}}{N_{\mathrm{c}}}<0.2, \tag{16}$$

where N_c is the design axial resistance of the member under pure compression, and $M_{z,c}$ and $M_{y,c}$ are the design bending moment resistances about the minor and major axes, respectively. Bending resistance is defined in AISC Design Guide 27 as a function of the local slenderness of the flanges and web. A slight anomaly in the calculation method was observed and resolved in [3], and the adjusted approach is employed herein.

Tables 9 and 10 show that the mean ratios of $N_u/N_{u,AISC}$ are equal to 1.06 and 1.17, with corresponding COVs equal to 0.18 and 0.18 for beam-columns with Class 1 and 2 cross-sections bending about the minor and major axes, respectively and 1.29 and 1.28, with corresponding COVs equal to 0.14 and 0.15 for beam-columns with Class 3 cross-sections bending about the minor and major axes, respectively. Overall, the AISC strength predictions are reasonable on average, but rather scattered and with a number of $N_u/N_{u,AISC}$ ratios on the unsafe side – see Figs. 18 and 19 for a graphical assessment of the AISC predictions for compression plus minor and major axis bending, respectively. The scatter is partly due to the adoption of a single buckling curve for instability about both the minor and major axes, while the over-predicted capacities stem from the shape of the interaction curve.

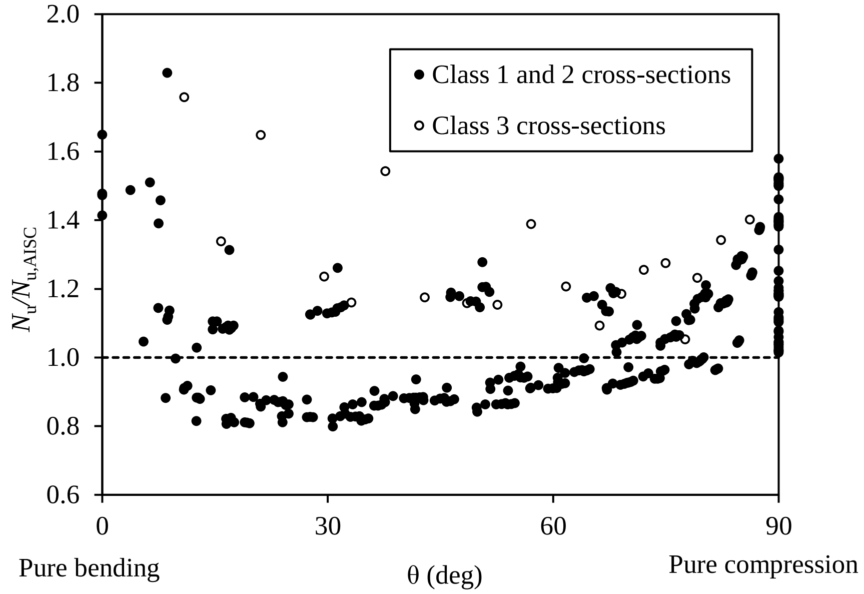

Fig. 18 Comparison of AISC strength predictions with beam-column test and FE results under compression and minor axis bending

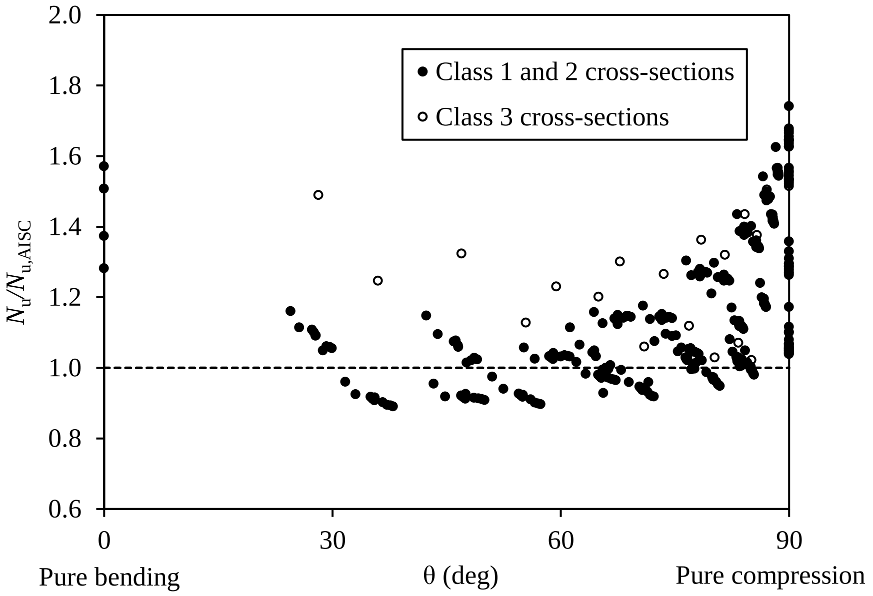

Fig. 19 Comparison of AISC strength predictions with beam-column test and FE results under compression and major axis bending

4.4 Greiner and Kettler's method

Greiner and Kettler[22] proposed new interaction buckling factors for stainless steel beam-columns with Class 1 and 2 cross-sections, following the general format of the interaction curves employed in Eurocode 3 for carbon steel beam-columns. Their design equations are given by Equations (17) and (18), while their proposed interaction factors $k_{G\&K,z}$ and $k_{G\&K,y}$, which were derived based on a set of generated numerical results, are given by Equations (19) and (20), for beam-columns under compression and bending about the minor and major axes, respectively.

$$\frac{N_{Ed}}{N_{b,z,Rd}}+k_{G\&K,z}\frac{M_{z,Ed}}{W_{pl,z}f_y}\leq 1, \tag{17}$$

$$\frac{N_{Ed}}{N_{b,y,Rd}}+k_{G\&K,y}\frac{M_{y,Ed}}{W_{pl,y}f_y}\leq 1, \tag{18}$$

$$k_{G\&K,z}=1.2+1.5\frac{N_{Ed}}{N_{b,z,Rd}}(\bar{\lambda}_z\text{-}0.7),\quad \text{but}\quad k_{G\&K,z}\leq 1.2+1.95\frac{N_{Ed}}{N_{b,z,Rd}}, \tag{19}$$

$$k_{G\&K,y}=0.9+2.2\frac{N_{Ed}}{N_{b,y,Rd}}(\bar{\lambda}_y\text{-}0.4),\quad \text{but}\quad k_{G\&K,y}\leq 0.9+2.42\frac{N_{Ed}}{N_{b,y,Rd}}. \tag{20}$$

The accuracy of Greiner and Kettler's proposals for the design of stainless steel I-section beam-columns is evaluated herein through comparisons of the experimental and numerical ultimate loads N_u with the predicted capacities $N_{u,G\&K}$. The mean ratios of $N_u/N_{u,G\&K}$, listed in Table 9, are 1.18 and 1.11, with the corresponding COVs equal to 0.12 and 0.05, for beam-columns with Class 1 and 2 cross-sections under compression and bending about the minor and major axes, respectively. Graphical comparisons of the ultimate loads from the tests (or FE models) and the predictions of Greiner and Kettler are shown in Figs. 20 and 21for compression plus minor axis and major axis bending, respectively, where the ratio of the test (or FE) ultimate loads to the predicted failure load ratio $N_u/N_{u,G\&K}$ is plotted against the angle parameter θ. It can be seen that Greiner and Kettler's proposals lead to improved results over the current Eurocode predictions, but that scope for further improvements remains.

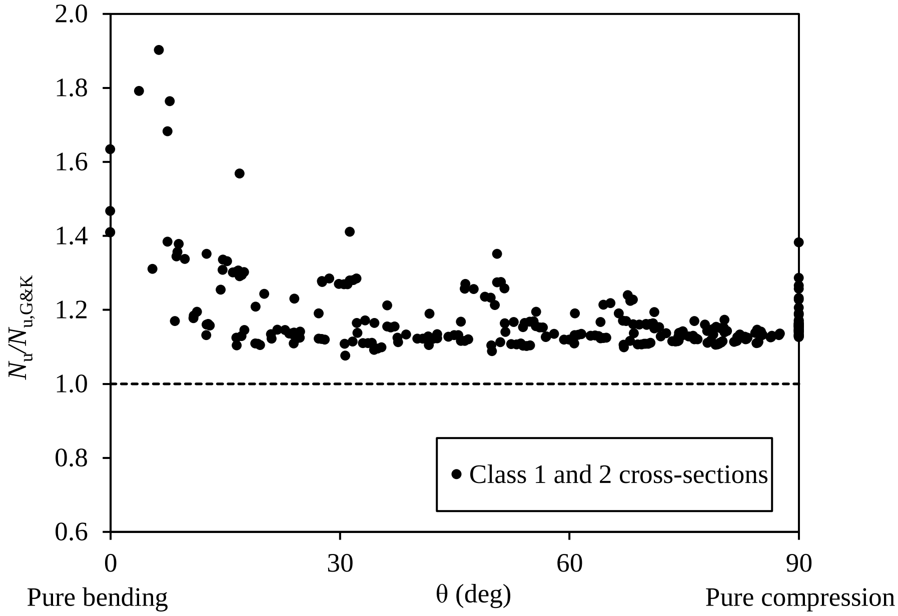

Fig. 20 Comparison of Greiner and Kettler's strength predictions with beam-column test and FE results under compression and minor axis bending

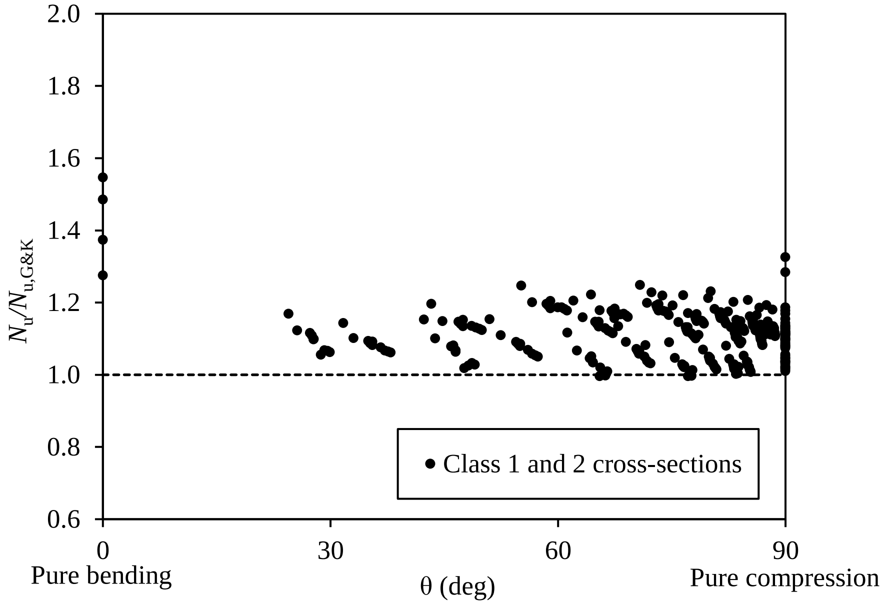

Fig. 21 Comparison of Greiner and Kettler's strength predictions with beam-column test and FE results under compression and major axis bending

5 New Proposal

Having observed some inaccuracy and scatter in the strength predictions of the existing provisions, improvements are sought in this section in two key areas: (1) the bending and column buckling end points and (2) the interaction factors.

For I-section members subjected to compression plus minor axis bending, the following interaction equation (Equation (21)) is proposed:

$$\frac{N_{\mathrm{Ed}}}{N_{\mathrm{b,z,Rd}}}+k_{\mathrm{csm,z}}\frac{M_{\mathrm{z,Ed}}}{M_{\mathrm{csm,z,Rk}}/\gamma_{\mathrm{M1}}}\leq 1, \tag{21}$$

while for compression plus major axis bending, where lateral torsional buckling is restrained, Equation (22) is proposed:

$$\frac{N_{\mathrm{Ed}}}{N_{\mathrm{b,y,Rd}}}+k_{\mathrm{csm,y}}\frac{M_{\mathrm{y,Ed}}}{M_{\mathrm{csm,y,Rk}}/\gamma_{\mathrm{M1}}}\leq 1, \tag{22}$$

where $k_{\mathrm{csm,z}}$ and $k_{\mathrm{csm,y}}$ are the interaction factors to be determined in this section, and $M_{\mathrm{csm,z,Rd}}$ and $M_{\mathrm{csm,y,Rd}}$ are the cross-section bending resistances about the minor and major axis, determined according to the continuous strength method (CSM) as given by Equations (23) and (24), respectively, and γ_{M1} is the partial safety factor for member buckling resistance.

$$M_{\mathrm{csm,z,Rk}} = W_{\mathrm{pl,z}}f_{\mathrm{y}}\left[1+\frac{E_{\mathrm{sh}}}{E}\frac{W_{\mathrm{el,z}}}{W_{\mathrm{pl,z}}}\left(\frac{\varepsilon_{\mathrm{csm}}}{\varepsilon_{\mathrm{y}}}-1\right)-\left(1-\frac{W_{\mathrm{el,z}}}{W_{\mathrm{pl,z}}}\right)\bigg/\left(\frac{\varepsilon_{\mathrm{csm}}}{\varepsilon_{\mathrm{y}}}\right)^{1.2}\right], \tag{23}$$

$$M_{\mathrm{csm,y,Rk}} = W_{\mathrm{pl,y}}f_{\mathrm{y}}\left[1+\frac{E_{\mathrm{sh}}}{E}\frac{W_{\mathrm{el,y}}}{W_{\mathrm{pl,y}}}\left(\frac{\varepsilon_{\mathrm{csm}}}{\varepsilon_{\mathrm{y}}}-1\right)-\left(1-\frac{W_{\mathrm{el,y}}}{W_{\mathrm{pl,y}}}\right)\bigg/\left(\frac{\varepsilon_{\mathrm{csm}}}{\varepsilon_{\mathrm{y}}}\right)^{2}\right], \tag{24}$$

where W_{pl} is the plastic section modulus, W_{el} is the elastic section modulus, $E_{\mathrm{sh}}=(f_{\mathrm{u}}-f_{\mathrm{y}})/(C_2\varepsilon_{\mathrm{u}}-\varepsilon_{\mathrm{y}})$ is the strain hardening slope with C_2=0.16 for austenitic stainless steel, $\varepsilon_{\mathrm{csm}}$ is the failure strain of cross-section predicted from the CSM base curve[37] and ε_{y} is the yield strain. A detailed description of the CSM can be found in [37] and [38]. Utilising the CSM to determine the bending moment resistance of the beam-columns ensures an accurate bending end point for the interaction curves and a sound basis for the derivation of the interaction factors. This is in contrast to the previous approaches, where the end points are often not well predicted and the derived interaction factors are partially compensating for this short coming[22, 39].

In terms of the column buckling end points, member resistances determined using recently proposed buckling curves in [4] were adopted, as given in Equations (25) to (27), with a plateau length $\bar{\lambda}_0$=0.2, and an imperfection factor α=0.76 and α=0.60 for laser-welded I-section columns buckling about the minor and major axis, respectively.

$$N_{\mathrm{b,Rd}} = \frac{\chi A f_{\mathrm{y}}}{\gamma_{\mathrm{M1}}}, \tag{25}$$

$$\chi = \frac{1}{\phi + \sqrt{\phi^2 - \bar{\lambda}^2}}, \tag{26}$$

$$\phi = \frac{1}{2}\left(1 + \alpha(\bar{\lambda} - \bar{\lambda}_0) + \bar{\lambda}^2\right). \tag{27}$$

Based on these more accurate end points, new interaction factors k_{csm} were derived, following a comprehensive numerical simulation programme, in a similar manner to in previous studies[39-41]. Numerical results obtained in the parametric studies described in Section 3.5, together with results from some supplementary models following the same modelling assumptions were used as the dataset for the derivation of the interaction factors. Individual interaction factors k_{csm} were calculated for each FE parametric data point from Equation (28) , which is simply a rearrangement of Equations (21) and (22),

$$k_{\mathrm{csm}}=\left(1-\frac{N_{\mathrm{Ed}}}{N_{\mathrm{b,Rd}}}\right)\frac{M_{\mathrm{csm,Rd}}}{M_{\mathrm{Ed}}}. \tag{28}$$

Seven compressive load levels ($n=N_{\mathrm{Ed}}/N_{\mathrm{b,Rd}}$), n = 0.2 to n = 0.8, in steps of 0.1, were considered. An example, for specimens under combined axial compression and major axis bending with n=0.6, of the relationship between the derived interaction factors k_{csm} and global slenderness $\bar{\lambda}$, is shown in Fig. 22. It can be observed that the curve shows a steeper slope in the low slenderness range but a relatively flat slope in the high slenderness range.

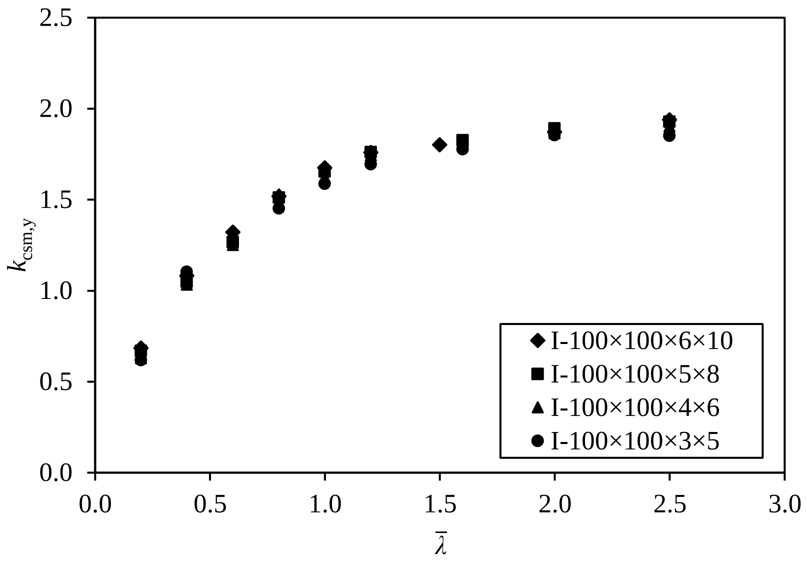

Fig. 22 Typical FE derived k_{csm} factors at load level n=0.6 for combined axial compression and major axis bending

Thus, the design expression for k_{csm} can assume the traditional bi-linear form given by Equation (29), as used in [40, 42] for carbon steel beam-column interaction factors and in [39, 41] for stainless steel interaction factors.

$$k_{csm} = 1+D_1\left(\bar{\lambda}\text{-}D_2\right)n, \text{ but } k_{csm} \leq 1+D_1(D_3\text{-}D_2)n, \tag{29}$$

where D_1 and D_2 are the coefficients that define the linear relationship between k_{csm} and global slenderness $\bar{\lambda}$ in the low member slenderness range when $\bar{\lambda} \leq D_3$, while D_3 is a limit value, beyond which the interaction factor k_{csm} remains constant.

The values of D_1 and D_2 for each load level n were determined following a regression fit of Equation (29) to the upper bound of the corresponding numerical dataset over the member slenderness range from 0.2 to 1.2. The average values of D_1 and D_2 for all load levels were determined and are tabulated in Table 11. The values of coefficient D_3 were determined by fitting Equation (29) to the upper bound of the dataset for low axial compressive load levels (i.e. $n \leq 0.4$) and are also listed in Table 11.

Table 11 Proposed interaction curve coefficients for austenitic stainless steel I-section beam-columns

Loading combinations	D_1	D_2	D_3
Compression and minor axis bending ($k_{csm,z}$)	2.80	0.50	1.2
Compression and major axis bending ($k_{csm,y}$)	2.50	0.35	1.0

The numerically derived and proposed curves for the interaction factors at various load levels n are compared in Figs. 23 and 24 for compression plus minor axis bending and compression plus major axis bending, respectively, with the dashed lines representing the upper bound curve obtained from the numerical results and the solid lines representing the design proposed curves.

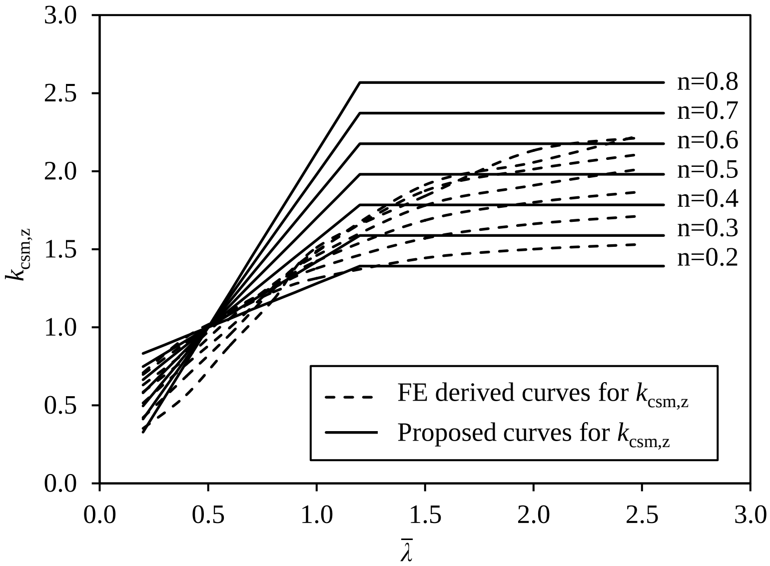

Fig. 23 Comparisons between the proposed and FE derived interaction factor curves for combined axial compression and minor axis bending

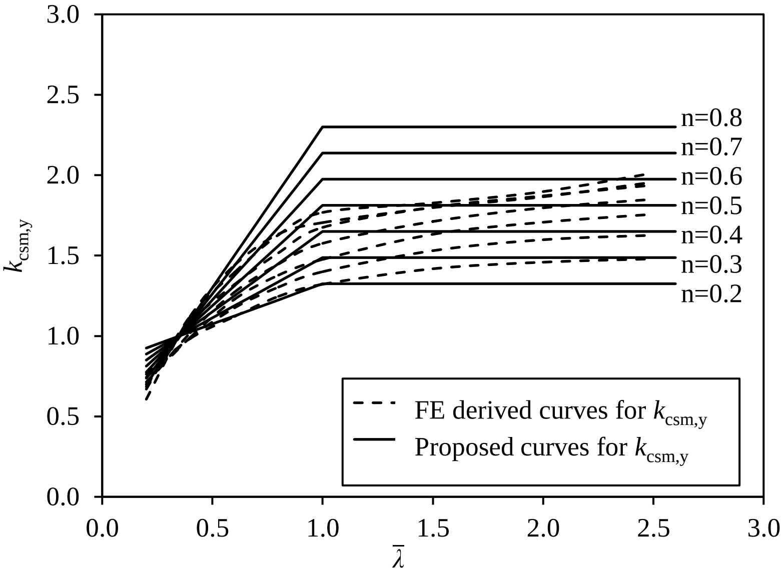

Fig. 24 Comparisons between the proposed and FE derived interaction factor curves for combined axial compression and major axis bending

From Figs. 23 and 24 it can be observed that there are relatively large discrepancies between the proposed and FE derived k_{csm} curves for high axial compressive load levels (*n* values) in the high member slenderness range (high $\bar{\lambda}$ values). However, the discrepancies are acceptable since for members with high slenderness and high axial load levels their structural response is controlled by column buckling, with the bending term which features k_{csm} having little influence on the prediction of the capacity. Similar observations were also made in [22, 39-41].

The proposed design interaction curves for beam-columns under axial compression and minor axis bending and axial compression and major axis bending for a range of member slenderness values are plotted in Figs. 25 and 26, respectively. As the member slenderness increases, second order effects become increasingly prominent, and thus, as expected the interaction curves become more concave.

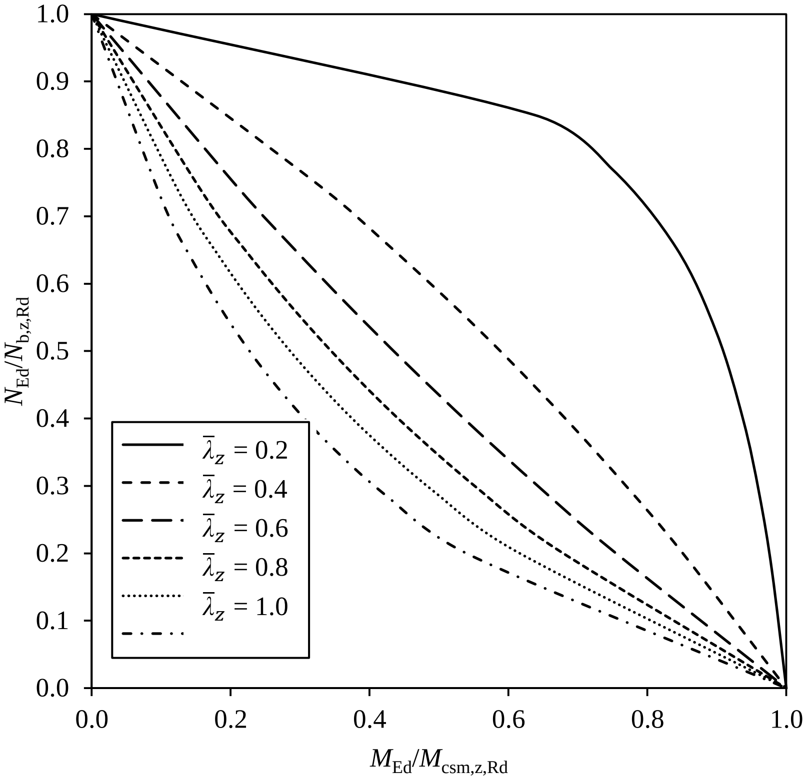

Fig. 25 Proposed design interaction curves for beam-columns under axial compression and minor axis bending with varying member slenderness

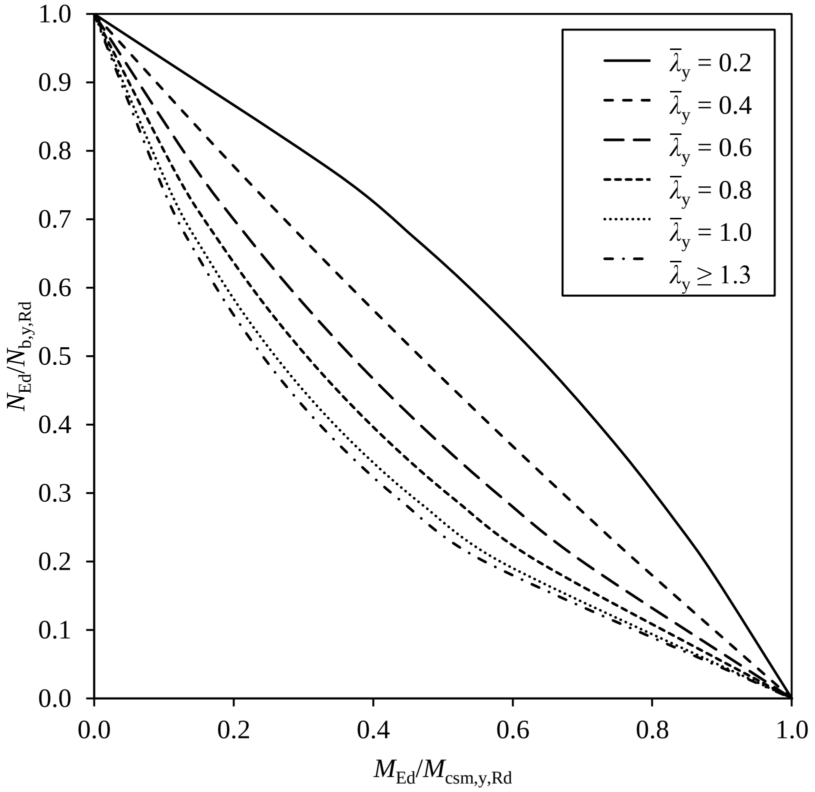

Fig. 26 Proposed design interaction curves for beam-columns under axial compression and major axis bending with varying member slenderness

The accuracy of the proposed design approaches was assessed through comparisons against the test and FE results, following a similar procedure to that employed in Section 4. The ratios of experimental (or numerical) failure loads to the predictions of the proposed method $N_u/N_{u,prop}$ are reported in Table 12. The mean ratios of $N_u/N_{u,prop}$ are equal to 1.10 and 1.08, for compression plus minor and major axis bending, respectively, with corresponding COVs equal to 0.08 and 0.04. The comparison is also shown in Figs. 27 and 28, where the test (or FE) to the predicted failure load ratios $N_u/N_{u,prop}$ are plotted against the angle parameter θ, for specimens under compression and minor axis bending and compression and major axis bending, respectively. The mean predictions and COV values may be seen to have been improved over those from the existing methods examined in Section 4, and there are only a very small number of predictions on the unsafe side.

Table 12 Comparison of beam-column test and FE results with predicted strengths from proposed approach

Loading combinations	No. of tests: 18 No. of simulations: 960	$N_u/N_{u,prop}$
Compression and bending about minor axis	Mean	1.10
	COV	0.08
Compression and bending about major axis	Mean	1.08
	COV	0.04

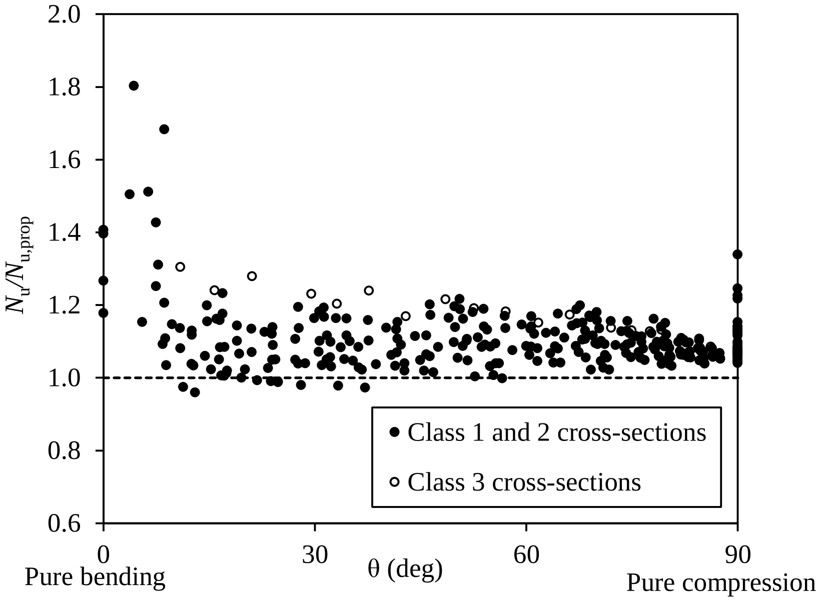

Fig. 27 Comparison of proposed strength predictions with beam-column test and FE results under compression and minor axis bending

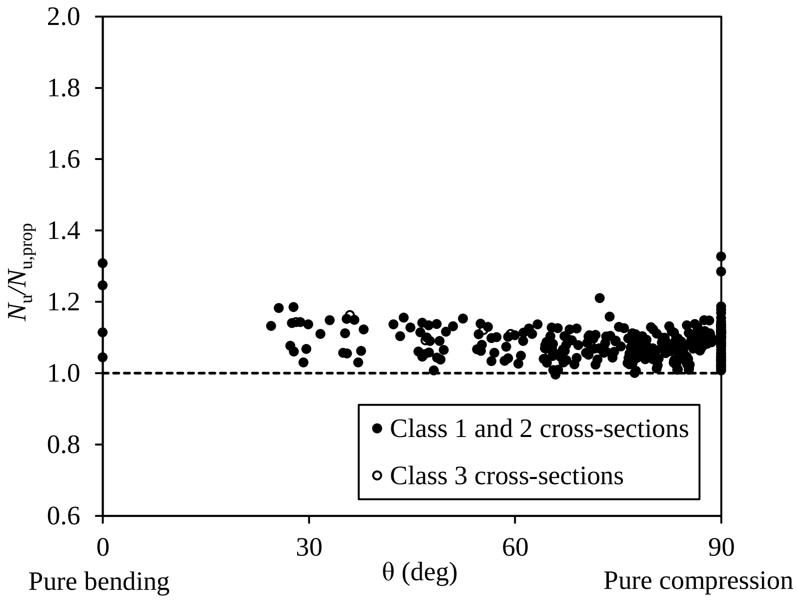

Fig. 28 Comparison of proposed strength predictions with beam-column test and FE results under compression and major axis bending

Statistical analyses in accordance with Annex D of EN 1990[43] were performed to assess the reliability of the proposed method. The key statistical parameters are presented in Table 13, where *n* is the size of the dataset, *b* is the mean value correction factor, $k_{d,n}$ is the fractile factor and is related to the size of the whole dataset and V_δ is the coefficient of variation of the test/FE capacities relative to the resistance model. Note that the parameter *b* is taken as the average of the ratios of the test and FE results to predicted resistances, which, unlike the least squares approach recommended in Annex D, does not bias the value of *b* towards the test or FE results with higher failure loads. The material over-strength factor and the coefficients of variation of the yield strength V_{fy} and geometry $V_{geometry}$ were taken as the values recommended by Afshan et al[44].

Table 13 Summary of statistical analysis results for proposed beam-column design approach

Loading combinations	Dataset	n	b	$k_{d,n}$	V_δ	γ_{M1}
Compression and bending about minor axis	Tests+FE	492	1.102	3.11	0.056	0.94
	Tests only	12	1.137	3.11	0.076	0.95
Compression and bending about major axis	Tests+FE	494	1.090	3.11	0.034	0.92
	Tests only	14	1.035	3.11	0.061	1.01

6 Conclusions

An experimental and numerical modelling investigation into the structural response of laser-welded austenitic stainless steel I-section beam-columns has been reported. The experimental investigation included eighteen tests on laser-welded stainless steel beam-columns under minor axis bending plus compression and major axis bending plus compression with lateral restraints. The test setups and experimental procedures were described. Numerical models were developed and validated against the test results obtained herein and from a previous study. Parametric studies were carried out to generate further structural performance data over a wide range of cross-section sizes, member non-dimensional slenderness and combinations of loading. The test and FE results were used to assess the accuracy and consistency of existing beam-column design provisions, including the European code EN 1993-1-4[20], American Institute of Steel Construction Design Guide 27[21] and Greiner and Kettler's proposals[22]. It was found that the European code generally led to relatively accurate design strength predictions, though were overly conservative in some instances; the AISC strength predictions showed good accuracy on average but with a high degree of scatter and some predictions on the unsafe side; Greiner and Kettler’s proposals offered improved predictions over EN 1993-1-4, though there remained scope for further improvement in the design of stainless steel I-section beam-columns. Hence, following analysis of the assembled experimental and numerical datasets, an improved approach for the design of stainless steel I-section beam-columns has been proposed and shown to offer more accurate and consistent capacity predictions.

Acknowledgements

The authors would like to thank Montanstahl AG for the supply of test specimens and financial support for the experimental programme. The financial support provided by the China Scholarship Council for Yidu Bu's PhD study is also gratefully acknowledged.

References

[1] Gardner L, Bu Y, Theofanous M. Laser-welded stainless steel I-sections: Residual stress measurements and column buckling tests. Engineering Structures. 2016;127:536-48.

[2] Theofanous M, Liew A, Gardner L. Experimental study of stainless steel angles and channels in bending. Structures. 2015;4:80-90.

[3] Bu Y, Gardner L. Local stability of laser-welded stainless steel I-sections in bending. Submitted to Journal of Constructional Steel Research. 2017.

[4] Bu Y, Gardner L. Finite element modelling and design of welded stainless steel I-section columns. Submitted. 2017.

[5] Yamada, Kato. Strength and deformation of H-shaped stainless steel beams. Japanese Institution of Architecture Journal of the Kanto branch. 1988.

[6] ECSC. ECSC project - Development of the use of stainless steel in construction. The Steel Construction Institute. 2000;Document RT810, Contract No. 720SA/842.

[7] Burgan BA, Baddoo NR, Gilsenan KA. Structural design of stainless steel members comparison between Eurocode 3, Part 1.4 and test results. Journal of Constructional Steel Research. 2000;54:51-73.

[8] Real E, Mirambell E. Flexural behaviour of stainless steel beams. Engineering Structures. 2005;27:1465-75.

[9] Saliba N, Gardner L. Cross-section stability of lean duplex stainless steel welded I-sections. Journal of Constructional Steel Research. 2013;80:1-14.

[10] Yang L, Wang Y, Gao B, Shi Y, Yuan H. Two calculation methods for buckling reduction factors of stainless steel welded I-section beams. Thin-Walled Structures. 2014;83:128-36.

[11] Wang Y, Yang L, Gao B, Shi Y, Yuan H. Experimental study of lateral-torsional buckling behavior of stainless steel welded I-section beams. International Journal of Steel Structures. 2014;14:411-20.

[12] Bredenkamp P, Van den Berg G. The strength of stainless steel built-up I-section columns. Journal of Constructional Steel Research. 1995;34:131-44.

[13] Becque J, Rasmussen KJ. Experimental investigation of the interaction of local and overall buckling of stainless steel I-columns. Journal of structural engineering. 2009;135:1340-8.

[14] Yuan HX, Wang YQ, Gardner L, Du XX, Shi YJ. Local–overall interactive buckling behaviour of welded stainless steel I-section columns. Journal of Constructional Steel Research. 2015;111:75-87.

[15] Yang L, Zhao M, Chan T-M, Shang F, Xu D. Flexural buckling of welded austenitic and duplex stainless steel I-section columns. Journal of Constructional Steel Research. 2016;122:339-53.

[16] Zheng B, Hua X, Shu G. Tests of cold-formed and welded stainless steel beam-columns. Journal of Constructional Steel Research. 2015;111:1-10.

[17] Zhao O, Gardner L, Young B. Testing and numerical modelling of austenitic stainless steel CHS beam–columns. Engineering Structures. 2016;111:263-74.

[18] Zhao O, Gardner L, Young B. Experimental study of ferritic stainless steel tubular beam-column members subjected to unequal end moments. Journal of Structural Engineering. 2016;142:04016091.

[19] Arrayago I, Real E, Mirambell E. Experimental study on ferritic stainless steel RHS and SHS beam-columns. Thin-Walled Structures. 2016;100:93-104.

[20] EN 1993-1-4:2006+A1:2015. Eurocode 3: Design of steel structures – Part 1.4: General rules supplmentary rules for stainless steels, including amendment A1 (2015). Brussels: European Committee for Standardization (CEN). 2015.

[21] AISC Design Guide 27: Structural Stainless Steel. American Institute of Steel Construction (AISC), Chicago, Illinois, USA 2013.

[22] Greiner R, Kettler M. Interaction of bending and axial compression of stainless steel members. Journal of Constructional Steel Research. 2008;64:1217-24.

[23] EN ISO 6892-1. Metallic materials – Tensile testing – Part 1: Method of test at room temperature. Brussels: European committee for standardization (CEN). 2009.

[24] Gardner L, Ashraf M. Structural design for non-linear metallic materials. Engineering Structures. 2006;28:926-34.

[25] Ziemian RD. Guide to stability design criteria for metal structures: John Wiley & Sons; 2010.

[26] Klopper JJ, Laubscher RF, Steuwer A, James MN. An investigation into the effect of weld technique on the residual stress distribution of 3CR12 (DIN 1.4003) built-up structural sections. Proceedings of the Institution of Mechanical Engineers, Part L: Journal of Materials Design and Applications 2011;225:123-32.

[27] Yuan HX, Wang YQ, Shi YJ, Gardner L. Residual stress distributions in welded stainless steel sections. Thin-Walled Structures. 2014;79:38-51.

[28] ECCS. European Convention for Constructional Steelwork. 1976.

[29] BSK99. Boverkets handbok om stalkonstruktioner, Swedish regulations for steel structures. 1999.

[30] Zhao O, Rossi B, Gardner L, Young B. Behaviour of structural stainless steel cross-sections under combined loading – Part I: Experimental study. Engineering Structures. 2015;89:236-46.

[31] ABAQUS. ABAQUS/Standard user's manual volumes I-III and ABAQUS CAE manual: Dassault Systemes Simulia Corporation; 2014.

[32] Theofanous M, Chan TM, Gardner L. Structural response of stainless steel oval hollow section compression members. Engineering Structures. 2009;31:922-34.

[33] Becque J, Lecce M, Rasmussen KJ. The direct strength method for stainless steel compression members. Journal of Constructional Steel Research. 2008;64:1231-8.

[34] Dawson RG, Walker AC. Post-buckling of geometrically imperfect plates. Journal of the Structural Division. 1972;98:75-94.

[35] Zhao O, Rossi B, Gardner L, Young B. Behaviour of structural stainless steel cross-sections under combined loading – Part II: Numerical modelling and design approach. Engineering Structures. 2015;89:247-59.

[36] EN 1993-1-1. Eurocode 3: Design of steel structures – Part 1.1: General rules and rules for buildings. Brussels: European Committee for Standardization (CEN). 2005.

[37] Afshan S, Gardner L. The continuous strength method for structural stainless steel design. Thin-Walled Structures. 2013;68:42-9.

[38] Zhao O, Afshan S, Gardner L. Structural response and continuous strength method design of slender stainless steel cross-sections. Engineering Structures. 2017;140:14-25.

[39] Zhao O, Gardner L, Young B. Behaviour and design of stainless steel SHS and RHS beam-columns. Thin-Walled Structures. 2016;106:330-45.

[40] Greiner R, Lindner J. Interaction formulae for members subjected to bending and axial compression in EUROCODE 3—the Method 2 approach. Journal of Constructional Steel Research. 2006;62:757-70.

[41] Buchanan C, Gardner L, Zhao O, Real E. Design of stainless steel CHS beam-columns. In: Heidarpour A, Zhao XL, editors. 16th International Symposium on Tubular Structures. Melbourne 2017.

[42] Boissonnade N, Greiner R, Jaspart J-P, Lindner J. Rules for Member Stability in EN 1993-1-1: Background documentation and design guidelines. ECCS European Convention for Constructional Steelwork; 2006.

[43] EN 1990. Basis of structural design. Brussels: European Committee for Standardization (CEN). 2002.

[44] Afshan S, Francis P, Baddoo N, Gardner L. Reliability analysis of structural stainless steel design provisions. Journal of Constructional Steel Research. 2015;114:293-304.